Needle Steering in Biological Tissue using Ultrasound-based Online Curvature Estimation

Pedro Moreira[1], Sachin Patil[2], Ron Alterovitz[3], and Sarthak Misra[1]

***Abstract*— Percutaneous needle insertions are commonly performed for diagnostic and therapeutic purposes. Accurate placement of the needle tip is important to the success of many needle procedures. The current needle steering systems depend on needle-tissue-specific data, such as maximum curvature, that is unavailable prior to an interventional procedure. In this paper, we present a novel three-dimensional adaptive steering method for flexible bevel-tipped needles that is capable of performing accurate tip placement without previous knowledge about needle curvature. The method steers the needle by integrating duty-cycled needle steering, online curvature estimation, ultrasound-based needle tracking, and sampling-based motion planning. The needle curvature estimation is performed online and used to adapt the path and duty cycling. We evaluated the method using experiments in a homogenous gelatin phantom, a two-layer gelatin phantom, and a biological tissue phantom composed of a gelatin layer and *in vitro* chicken tissue. In all experiments, virtual obstacles and targets move in order to represent the disturbances that might occur due to tissue deformation and physiological processes. The average targeting error using our new adaptive method is 40% lower than using the conventional non-adaptive duty-cycled needle steering method.**

I. Introduction

Needle insertion in soft tissues is a common step in many minimally invasive medical procedures. Clinical needle-based interventions are used in therapeutic and diagnostic procedures, including biopsy, brachytherapy, and neurosurgery [1]. Needle placement accuracy is crucial for the success of many procedures, and misplacement of the needle tip may cause misdiagnosis or unsuccessful treatment. During needle insertion, the interaction of the needle with tissue as well as physiological processes such as respiration can cause the clinical target to move. Target motion, tissue inhomogeneities, and unexpected needle/tissue interaction forces can cause disturbances that contribute to needle placement errors.

[1]Pedro Moreira and Sarthak Misra are affiliated with MIRA - Institute for Biomedical Technology and Technical Medicine (Robotics and Mechatronics), University of Twente, The Netherlands. {p.lopesdafrotamoreira,s.misra}@utwente.nl

[2]Sachin Patil is with the Department of Electrical Engineering and Computer Sciences, University of California at Berkeley, USA. sachinpatil@berkeley.edu

[3]Ron Alterovitz is with the Department of Computer Science, University of North Carolina at Chapel Hill, USA. ron@cs.unc.edu

This research was supported by funds from the Dutch Ministry of Economic Affairs and the Province of Overijssel, within the Pieken in de Delta (PIDON) Initiative, Project MIRIAM (Minimally Invasive Robotics In An MRI environment). This research was also supported by the United States National Science Foundation (NSF) under award IIS-1149965 and by the United States National Institutes of Health (NIH) under award R21EB017952.

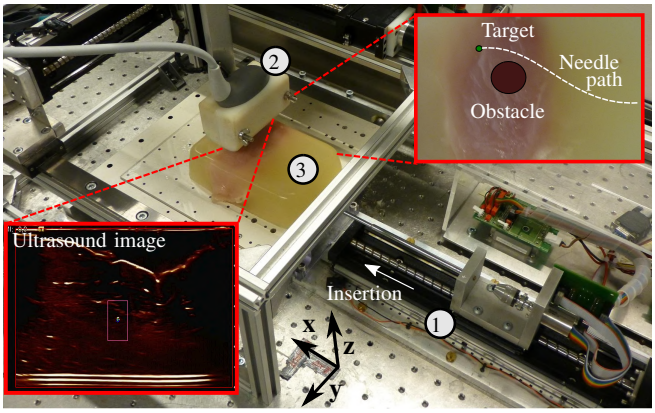

Fig. 1. A robotic device inserts and axially rotates a bevel-tipped flexible needle into a phantom. An ultrasound-based needle tracker estimates the needle tip pose and a motion planning algorithm computes a feasible needle path to the target. (1) Needle insertion device. (2) Ultrasound transducer. (3) Biological tissue phantom composed of gelatin and biological tissue.

Steerable needles have been introduced to enable clinicians to reduce needle placement errors and maneuver around anatomical obstacles by steering the needle during insertion [2]. Bevel-tipped flexible needles, the class of steerable needles we focus on in this paper, naturally bend when they are inserted through soft tissue. A kinematic model for flexible bevel-tipped needles based on the nonholonomic unicycle model was developed by Webster et al. [3]. This kinematic model relates needle insertion velocities and tip position assuming that the needle bends in a circular path with constant curvature. In order to achieve paths with different curvatures, Engh et al. [4] introduced the technique of duty cycled spinning of the needle.

Current models of needle steering require needle-tissue-specific data, such as the needle's maximum curvature, that is typically unavailable or uncertain prior to an interventional procedure. In current systems for flexible needle steering, the maximum curvature is typically estimated by performing a series of pre-operative insertions. It is clear that performing extra needle insertions to estimate the maximum curvature contradicts the idea of minimally invasive surgery. Moreover, biological tissues are rarely homogeneous and the needle's maximum curvature might vary during the insertion. Therefore, online estimation of the needle's maximum curvature is important to enable accurate needle tip placement using steerable needles.

Needle steering systems combining the nonholonomic model proposed by Webster et al. [3] and the duty cycling

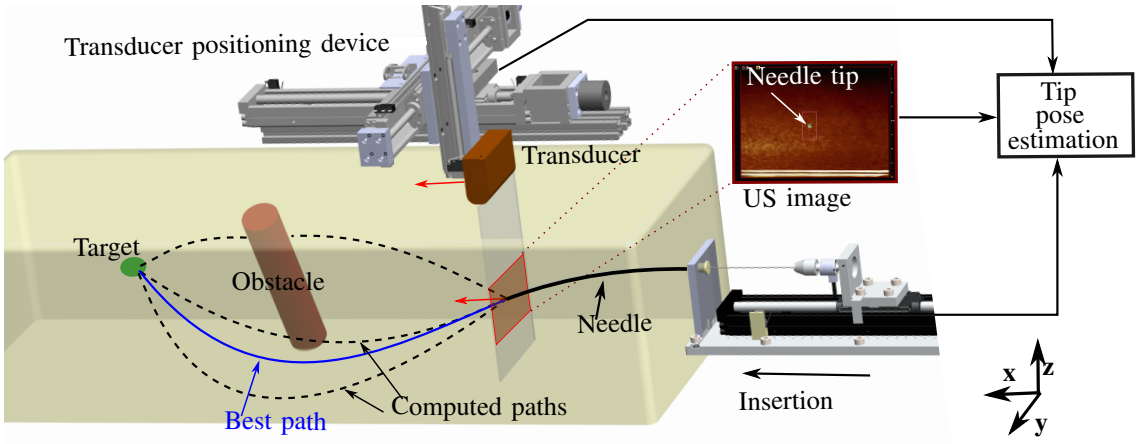

Fig. 2. Needle tracking and path planning: The ultrasound (US) transducer is robotically positioned on the same plane as the needle tip. The tip pose is estimated using the information from the US image, the needle insertion device, and the transducer positioning device. The needle pose is used by the motion planner at each re-planning step to generate many feasible paths to the target. The planner selects the best path such that the needle path length is minimized while avoiding obstacles.

technique were presented by Minhas et al. [5] and Wood et al. [6]. Wood et al. [6] also implemented a nonlinear control algorithm for path tracking using charge-coupled device (CCD) cameras to provide the needle tip position and orientation. The needle path is computed based on pre-operative information, such as the insertion point and locations of the obstacles and the target. However, the aforementioned work does not consider obstacle and target motions that may occur during a needle insertion procedure. Xu et al. [7] and Patil and Alterovitz [8] presented path planning algorithms for steerable needles based on the Rapidly-Exploring Random Tree (RRT) algorithm in order to enable avoidance of obstacles. The planners were validated through simulation studies. Bernardes et al. [9] presented experiments with two-dimensional (2D) needle insertions using RRT-based path planning and duty-cycled rotations. The needle tip position was estimated using a CCD camera. The use of CCD cameras as an imaging modality creates a drawback for clinical implementations. Additionally, the state of the art duty-cycled steering algorithms require previous knowledge of the maximum needle curvature during the insertion. The needle curvature depends on many factors, such as tissue stiffness, needle diameter, and bevel-tip angle. In addition, the current duty-cycled needle steering methods assume that the environments are homogeneous and maximum needle curvatures are constant. However, biological tissues are inhomogeneous [10].

This work proposes a novel three-dimensional (3D) adaptive duty-cycled needle steering approach able to cope with inhomogeneous tissues and unknown tissue properties. The approach estimates online the needle's curvature based on the needle tip's motion and adaptively updates the path and duty cycling. The system integrates a 3D ultrasound-based needle tracker [11] and RRT-based path planning [8]. Experiments steering a flexible needle toward a moving target on two-layer gelatin phantoms and biological tissue phantoms are presented in order to validate the proposed method (Fig. 1).

The paper is organized as follows. In Section II, the adaptive steering method is described. Section III presents the experimental setup and results, followed by Section IV, which concludes and provides directions for future work.

II. Methods

First, we present the needle tracking and path planning methods. Subsequently, we describe the needle steering method based on duty-cycled spinning of the needle. Finally, we present the online curvature estimation method.

A. Ultrasound-based needle tracking and path planning

The needle tip pose is estimated using a 2D ultrasound transducer. The transducer is placed perpendicular to the needle tip to measure its position (Fig. 2). During the needle insertion, the transducer is robotically repositioned to track the needle tip. The transducer is positioned by a robotic device that uses the insertion velocity corrected by tip velocities to determine out-of-plane motion [12]. An image processing algorithm is used to estimate the needle tip position from the ultrasound image by applying basic image processing techniques such as median filtering, thresholding, erosion, and dilation [11]. The needle tracking frequency is 25 Hz and the maximum mean errors in needle tip positions are 0.64 mm, 0.25 mm, and 0.27 mm along the x-, y-, and z-axes, respectively.

The path planner computes a feasible path to a specified target from the needle tip pose provided by the ultrasound-based tracker. We use the steerable needle motion planning algorithm introduced by Patil and Alterovitz [8]. We adapted the motion planner to use the needle tip pose estimated by the ultrasound-based tracker. The objective of the motion planner is to compute a feasible needle path from the current state to the target while avoiding obstacles. The motion planner is executed repeatedly at a frequency of 1 Hz until the target is reached. At each re-planning step, the motion planner generates many plans (typically hundreds) and selects the plan that best fulfills user-specified criteria, which in our

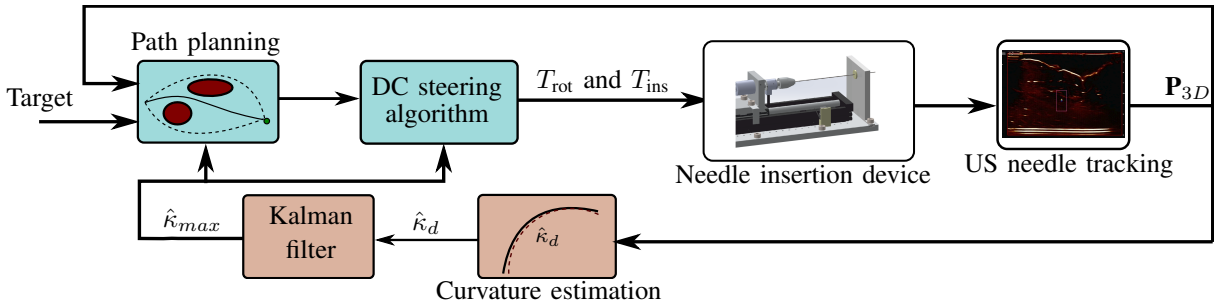

Fig. 3. The overall system diagram. The needle insertion device rotates and inserts the needle with rotation periods (T_{rot}) and insertion periods (T_{ins}) defined by the duty-cycled (DC) steering algorithm. The desired needle path is computed by the Rapidly-Exploring Random Tree (RRT) motion planning algorithm. The needle curvature ($\hat{\kappa}_{\text{d}}$) and the maximum curvature ($\hat{\kappa}_{\text{max}}$) are defined by the estimation algorithm. $\mathbf{P}_{3D}$ is the needle tip position estimated by the ultrasound (US) needle tracker.

implementation is minimizing the length of the needle path while avoiding obstacles.

The planned motion is composed of arcs with specified curvatures (κ_{d}) that can vary from the maximum curvature to a straight path. The curvature specified by the motion planner is then passed to the duty-cycled needle steering controller.

B. Duty-cycled needle steering control

The duty cycling technique is based on the idea of inserting and rotating the needle simultaneously to provide different needle curvatures during the insertion. The method works by alternating insertion periods with and without high-speed needle rotation. The needle moves straight when it is inserted and rotated at the same time. If no rotation is applied during the insertion the needle follows a path with maximum curvature ($\kappa = \kappa_{\text{max}}$). The proportion of the time spent rotating (T_{rot}) relative to the time spent inserting (T_{ins}) is called the duty cycle factor (α), and it is given by [5]

$$\alpha = \frac{T_{\text{rot}}}{T_{\text{rot}} + T_{\text{ins}}}. \tag{1}$$

In some phantoms this factor is related to the desired needle curvature (κ_{d}) and the maximum curvature (κ_{max}) by

$$\kappa_{\text{d}} = \kappa_{\text{max}}(1 - \alpha). \tag{2}$$

In the proposed steering algorithm, the maximum curvature (κ_{max}) is estimated and updated online.

C. Curvature estimation and online adaptation

In this subsection we present the method to adapt the relationship between desired curvature (κ_{d}) and duty cycle factor (α). An online curvature estimation is performed, followed by a maximum curvature adaptation. The overall control scheme is depicted in Fig. 3.

The curvature estimation is performed by defining the needle path as a series of arcs with constant curvatures. Each arc is considered as a sub-trajectory. This sub-trajectory is defined by one duty-cycling period, which is 1 second and has 30 tip pose measurements. A least squares algorithm is used to estimate the radius of curvature at each sub-trajectory. The 3D curvature estimation problem is transformed into a series of 2D problems (Fig. 4). The principal component analysis (PCA) is used to find the plane where the sub-trajectory path is performed.

A fast PCA algorithm is implemented by using singular value decomposition (SVD), as presented in Algorithm 1. The planar motion of the needle tip is given by the projected data-set ($\mathbf{P}_{2D}$). A least squares fitting of a circle is performed in order to estimate the curvature ($\hat{\kappa}_d$) for each sub-trajectory.

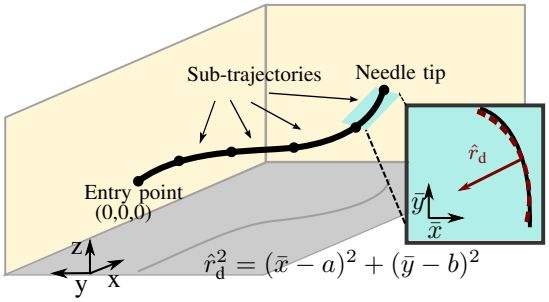

Fig. 4. The needle path is divided into sub-trajectories. In each sub-trajectory the needle follows a circular path, and the radius of curvature ($\hat{r}_{\text{d}}$) is estimated by a circle fitting algorithm. The center of the circle has coordinates (a, b).

Algorithm 1 PCA using SVD

for $i = 0 : N$ **do**
  $\mathbf{P}_{3D}(i,1) \leftarrow$ tip_position_x(i)
  $\mathbf{P}_{3D}(i,2) \leftarrow$ tip_position_y(i)
  $\mathbf{P}_{3D}(i,3) \leftarrow$ tip_position_z(i)
end for
$\bar{\mathbf{P}}_{3D} \leftarrow \mathbf{P}_{3D} -$mean$(\mathbf{P}_{3D})$ {subtract the mean value}
[**U**, Σ, **V**] $\leftarrow$svd$(\bar{\mathbf{P}}_{3D})$ {SVD decomposition}
$\mathbf{P}_{2D} \leftarrow \mathbf{U}^T\mathbf{P}_{3D}$ {project the 3D data}
$\hat{r}_d \leftarrow$ circlefitting$(\mathbf{P}_{2D})$ {Least squares circle fitting}
$\hat{\kappa}_d \leftarrow 1/\hat{r}_d$

The estimated needle curvature ($\hat{\kappa}_{\text{d}}$) and the applied duty cycle factor (α) are used to calculate the maximum needle curvature (κ_{max}). Accurately fitting a circle to the needle path is difficult when the needle path approaches a straight line. In addition, errors in sensing the tip position induce noise in the radius of curvature estimation. To address these difficulties, we use a Kalman Filter (KF) [13] to estimate the maximum

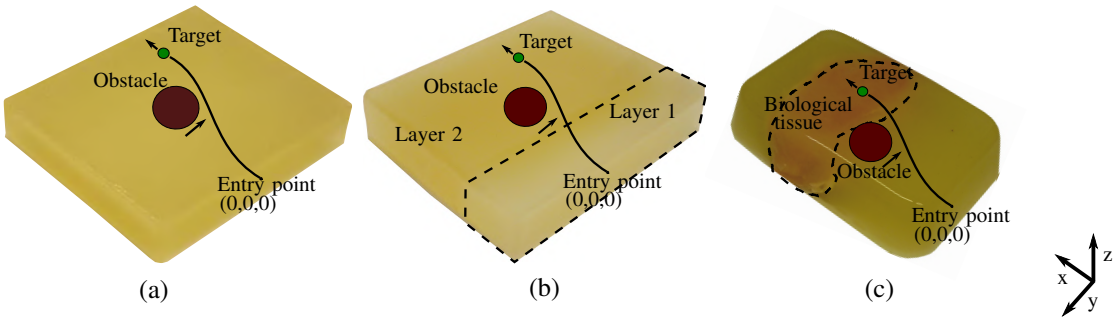

Fig. 5. Experimental phantoms and scenarios. (a) Scenario 1, experiments performed in a homogenous phantom. (b) Scenario 2, experiments performed in a two-layer phantom. (c) Scenario 3, experiments performed in a biological tissue phantom. In all experiments the initial target location is set to $x = 90$ mm, $y = -15$ mm, and $z = -5$ mm.

curvature ($\kappa_{\max}$). We define a discrete system based on (2) with estimated curvature ($\hat{\kappa}_{\mathrm{d}}$) as an output. The matrices for state space representation are

$$y = \hat{\kappa}_{\mathrm{d}},\ \mathbf{x} = \begin{bmatrix} \hat{\kappa}_{\mathrm{d}} & \kappa_{\max} \end{bmatrix}^T,\ \mathbf{C} = \begin{bmatrix} 1 & 0 \end{bmatrix} \text{ and}$$

$$\mathbf{A} = \begin{bmatrix} 0 & (1-\alpha) \\ 0 & 1 \end{bmatrix}.$$

The state estimation is given by

$$\hat{\mathbf{x}}(k+1) = \mathbf{A}\hat{\mathbf{x}}(k) + \mathbf{K}(k)e(k) \tag{3}$$

where $\hat{\mathbf{x}}$ is the estimated state vector, $\mathbf{K}(k)$ is the Kalman gain, and $e = \hat{\kappa}_{\mathrm{d}} - \mathbf{C}\hat{x}(k)$. For the experiments presented in this work the KF is experimentally tuned with system covariance 7×10^{-6} and measurement covariance 4×10^{-4}. The KF estimates the maximum curvature ($\kappa_{\max}$), which is used to adapt the duty-cycled needle steering algorithm.

III. Experiments

In this section, we describe the experiments performed to evaluate the adaptive needle steering method. The experimental results are also presented in this section.

A. Experimental scenarios

Experiments are conducted to validate the adaptive needle steering method. The needle is steered to a target in a non-static environment while avoiding obstacles. The experiments are performed with moving obstacles and targets to mimic the displacements caused by tissue deformation and physiological processes. No previous insertions were performed to estimate the maximum needle curvature. The initial value for the maximum radius of curvature is set to 270 mm ($\kappa_{\max} = 0.0037$ mm^{-1}) for all experiments. This value was reported by Abayazid et al. [14] as the maximum radius of curvature in gelatin phantoms that are similar to the ones used in this work. Our proposed adaptive method is evaluated under three different experimental scenarios (Fig. 5):

1) Homogenous phantom: The needle is steered towards a moving target in a homogeneous phantom while avoiding a moving obstacle. In this experimental scenario we evaluate targeting accuracy when the needle's maximum curvature is unknown.
2) Two-layer phantom: The needle is steered towards a moving target in a two-layer phantom while avoiding a moving obstacle. The first layer is made softer than the second layer. The different elastic properties of each layer change the maximum radius of curvature. The goal of this scenario is to evaluate our method under abrupt changes in elastic properties.
3) Biological tissue phantom: The needle is steered towards a moving target in a two-layer phantom composed of gelatin and biological tissue. The goal of this experimental scenario is to evaluate the targeting accuracy in biological tissues.

B. Experimental setup

The experimental setup used to steer the needles into phantoms is shown in Fig. 1. The needle insertion device has two degrees of freedom: translation along and rotation about the insertion axis [15]. During the needle insertion, ultrasound-based tracking (Transducer 18L6HD, Siemens ACUSON S2000 ultrasound system, Siemens AG, Erlangen, Germany) is used to estimate the needle tip pose. The needle used in the experiments is made of Nitinol ($E = 75$ GPa). It is a solid wire with diameter of 1 mm and has a bevel tip angle of 30°.

The needle is inserted in phantoms prepared with a mixture of water, gelatin (Dr.Oetker, Ede, The Netherlands), and silica gel 63 (E. Merck, Darmstadt, Germany). The Young's modulus of each phantom is estimated using an ultrasound-based Acoustic Radiation Force Impulse (ARFI) imaging technique. The shear wave propagation speed is measured using a commercially-available implementation of the ARFI imaging technique, known as Virtual Touch$^{\mathrm{TM}}$ Quantification, available on the Siemens ACUSON S2000 ultrasound system. The Young's modulus (E) is calculated as

$$E = 2\rho v_s^2(1+\mu), \tag{4}$$

where μ is the Poisson's ratio, ρ is the density, and v_s is the shear wave propagation speed [16].

The phantoms are prepared with elastic properties similar to human tissues to provide a more realistic clinical scenario. The homogeneous phantom is prepared with 84% water, 15% gelatin, and 1% silica. The Young's modulus of this

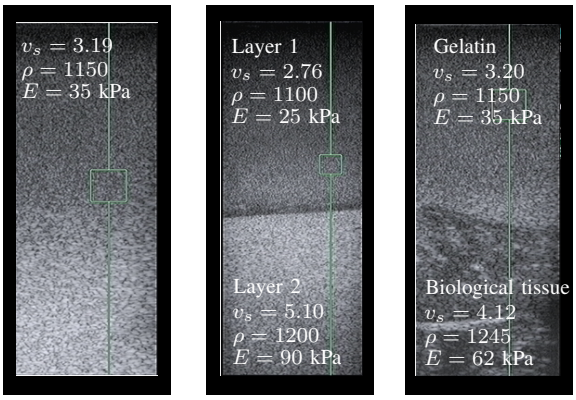

Fig. 6. Ultrasound-based acoustic radiation force impulse imaging technique used in the elasticity estimation for all three phantoms. The Poisson's ratio (ρ) is assumed to be 0.495. (a) Homogeneous phantom; (b) Two-layer phantom, and (c) Biological tissue phantom.

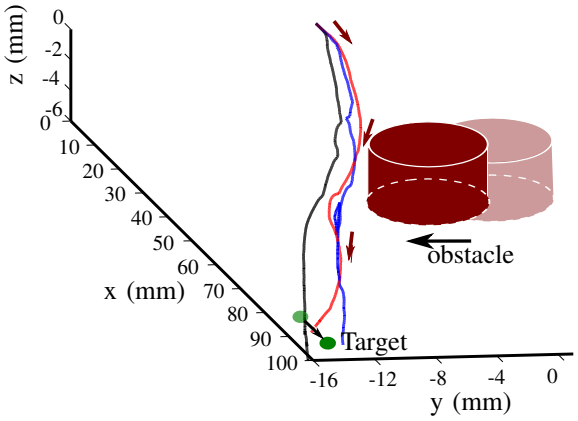

Fig. 7. Representative experimental results steering a bevel-tipped flexible needle towards a moving target while avoiding a moving obstacle. Red line is the result in a homogeneous phantom (Scenario 1), black line is the result in a two-layer phantom (Scenario 2) and blue line is the result in a biological tissue phantom (Scenario 3). *Please refer to the accompanying video that demonstrates the experimental results.*

phantom is calculated to be 35 kPa, which is similar to human breast tissue [17]. The first layer of the two-layer phantom is prepared with 90% water, 9% gelatin, and 1% silica, which results in $E \approx 25$ kPa. The second layer has 80% water, 19% gelatin, 1% silica, and $E \approx 90$ kPa. The two-layer phantom has elasticity similar to a normal fat tissue ($E \approx 22$ kPa) and a cancerous prostate ($E \approx 96$ kPa) [18]. The biological tissue phantom is composed of a layer of gelatin (with the same concentration as the homogeneous phantom) and a layer of *in vitro* chicken breast tissue (Fig. 5c). The ultrasound ARFI images for all three phantoms are presented in Fig. 6. The phantoms are maintained at 7° C for at least 5 hours before the experiments are performed.

C. Results

The needle is inserted with a velocity of 3 mm/s. The initial virtual target location for all experiments is $x = 90$ mm, $y = -15$ mm, and $z = -5$ mm. After 20 s of needle insertion, the target starts to move with a constant velocity of 0.4 mm/s along the x-axis until the needle reaches the target. The target depth of 90 mm is within the range of typical biopsy depths of prostate lesions and tumors which are approximately between 50 to 90 mm [19]. The insertion stops when the needle tip and target positions in the x-axis are equal. The obstacle is defined to simulate a bone of 20 mm diameter, and located at $x = 55$ mm, $y = 5$ mm, and $z = 0$ mm. The obstacle moves along the y-axis during the first 10 s with a constant velocity of 0.3 mm/s. The obstacle movement simulates displacements on sensitive tissues that might happens due to physiological processes.

Six experiments are performed for each scenario, three using our adaptive method and three using the conventional duty-cycled steering algorithm, i.e., without adaptation. The results are summarized in Table I. One experimental result for each scenario is given in Fig. 7. Further, the evolution of the estimated maximum needle curvature ($\kappa_{\max}$) is presented in Fig. 8. The maximum curvature varies as the needle crosses the interface between layers. In Scenario 2, the variation of the estimated maximum curvature is abrupt since the needle enters a stiffer environment. In Scenario 3, this variation is smooth since the needle enters an inhomogeneous biological tissue. Although the initial value of maximum curvature is defined based on previous reported values in Abayazid et al. [14], one can observe that after the insertion starts the estimated maximum curvature increases. This happens because even with the same gelatin concentration, other aspects influence the maximum curvature, such as the temperature that the phantoms were stored and the age of the gelatin. The experimental results in Scenario 1 show that using our adaptive method the average targeting error is 46% lower than using the non-adaptive method. Our adaptive method was able to reduce the targeting error by 53% in the two-layer phantom experiments. The experiments in biological tissue phantom show that our method achieved a targeting error 39% lower than using the non-adaptive method.

The results show that the targeting accuracy of duty-cycled needle steering was improved in all three scenarios. The average errors in Scenario 2 show that our adaptive method is able to cope with changes in the phantom elastic properties. In some experiments of Scenario 3 when the needle was inside the biological tissue, the tracking algorithm could not distinguish the needle tip from internal structures of the tissue, which induce errors in the tip position estimation. Improvements in the needle tracking system will reduce the final targeting error.

TABLE I

RMS TARGETING ERRORS AND STANDARD DEVIATIONS IN ALL EXPERIMENTAL SCENARIOS

Scenario	Targeting error (mm)	
	Without adaptive method	With adaptive method
1	1.88 ± 0.82	1.02 ± 0.73
2	2.35 ± 0.80	0.98 ± 0.23
3	3.15 ± 1.02	2.46 ± 0.81

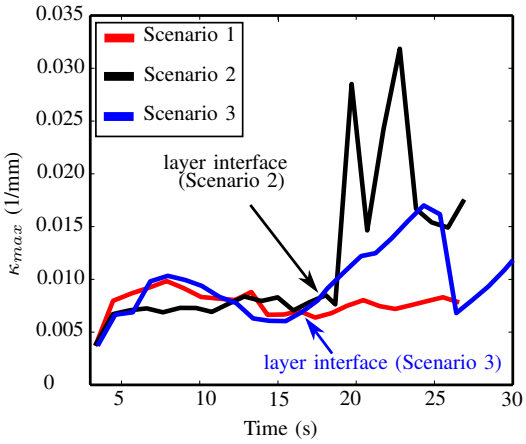

Fig. 8. Estimated maximum curvature during the needle steering experiments. The red line is the curvature estimation in the homogeneous gelatin phantom (Scenario 1), the black line is the curvature estimation in the two-layer gelatin phantom (Scenario 2), and the blue line is the curvature estimation in the biological tissue phantom composed of gelatin and *in vitro* chicken breast tissue (Scenario 3).

IV. Conclusion

We presented an adaptive method to steer a bevel-tipped flexible needle to a moving target in inhomogeneous phantoms while avoiding a moving obstacle. The system integrates ultrasound-based needle tracking, RRT-based path planning, and an online curvature estimation algorithm. The results show that our method was able to perform needle tip placement in three different scenarios: a homogeneous gelatin phantom, a gelatin phantom with two different elastic properties, and a biological tissue phantom composed of a gelatin layer and an *in vitro* chicken tissue, where average targeting errors for the three experimental scenarios were 1.02 mm, 0.98 mm, and 2.46 mm, respectively. The results in all three scenarios demonstrate that our method was able to reduce the targeting error by approximately 40% when compared to the non-adaptive duty-cycled method. The targeting errors are in the same range as the smallest target that can be detected using ultrasound images, which is typically 2 mm [14]. The results indicate that the online adaptation can be used to perform needle steering without previous knowledge of needle curvature. The results also demonstrate the system's ability to cope with multi-layer gelatin phantoms and biological tissues.

Future work will focus on improving the ultrasound-based needle tracking to increase its robustness by including a needle deflection model in the tip position estimation algorithm. More experiments are planned to investigate the influence of insertion velocity and obstacle motion on the targeting accuracy. We are currently adapting our transducer positioning device to move on curved surfaces which will allow us to perform *in vivo* studies. We will also investigate the relationship between the Young's modulus of the tissue and the maximum radius of curvature. Our current study demonstrates that it is possible to improve the accuracy of needle tip placement by using an online adaptive steering method.

References

[1] T. K. Podder, D. P. Clark, J. Sherman, D. Fuller, E. M. Messing, D. J. Rubens, J. G. Strang, Y. D. Zhang, W. O'Dell, W. S. Ng, and Y. Yu, "Effects of tip geometry of surgical needles: An assessment of force and deflection," in *European Medical and Biological Engineering Conference (EMBEC)*, Prague, Czech Republic, November 2005.

[2] N. Abolhassani, R. Patel, and M. Moallem, "Needle insertion into soft tissue: A survey," *Medical Engineering & Physics*, vol. 29, no. 4, pp. 413 – 431, 2007.

[3] R. J. Webster III, J. S. Kim, N. J. Cowan, G. S. Chirikjian, and A. M. Okamura, "Nonholonomic modeling of needle steering," *The International Journal of Robotics Research*, pp. 509 – 525, 2006.

[4] J. Engh, G. Podnar, S. Khoo, and C. Riviere, "Flexible needle steering system for percutaneous access to deep zones of the brain," in *Proceedings of the IEEE Annual Northeast Bioengineering Conference*, April 2006, pp. 103 – 104.

[5] D. S. Minhas, J. A. Engh, M. M. Fenske, and C. N. Riviere, "Modeling of needle steering via duty-cycled spinning," in *Proceedings of the Annual International Conference of the IEEE Engineering in Medicine and Biology Society (EMBC)*, Buenos Aires, Argentina, August 2007, pp. 5432 – 5435.

[6] N. A. Wood, K. Shahrour, M. C. Ost, and C. N. Riviere, "Needle steering system using duty-cycled rotation for percutaneous kidney access," in *Proceedings of the Annual International Conference of the IEEE Engineering in Medicine and Biology Society (EMBC)*, Buenos Aires, Argentina, September 2010, pp. 5432 – 5435.

[7] J. Xu, V. Duindam, R. Alterovitz, and K. Goldberg, "Motion planning for steerable needles in 3D environments with obstacles using rapidly-exploring random trees and backchaining," in *Proceedings of the IEEE International Conference on Automation Science and Engineering (CASE)*, Arlington, USA, August 2008, pp. 41 – 46.

[8] S. Patil and R. Alterovitz, "Interactive motion planning for steerable needles in 3D environments with obstacles," in *Proceedings of the IEEE RAS and EMBS International Conference on Biomedical Robotics and Biomechatronics (BioRob)*, Tokyo, Japan, September 2010, pp. 893 – 899.

[9] M. Bernardes, B. Adorno, P. Poignet, and G. Borges, "Robot-assisted automatic insertion of steerable needles with closed-loop imaging feedback and intraoperative trajectory replanning," *Mechatronics*, vol. 23, no. 6, pp. 630 – 645, 2013.

[10] S. Misra, K. T. Ramesh, and A. M. Okamura, "Needle insertion into soft tissue: A survey," *Presence: Teleoperators and Virtual Environments*, vol. 17, no. 5, pp. 463 – 491, 2008.

[11] G. J. Vrooijink, M. Abayazid, and S. Misra, "Real-time three-dimensional flexible needle tracking using two-dimensional ultrasound," in *Proceedings of the IEEE International Conference on Robotics and Automation (ICRA)*, Karlsruhe, Germany, May 2013, pp. 1680 – 1685.

[12] G. J. Vrooijink, M. Abayazid, S. Patil, R. Alterovitz, and S. Misra, "Needle path planning and steering in a three-dimensional non-static environment using two-dimensional ultrasound images," *International Journal of Robotics Research (In Proof)*, 2014.

[13] G. C. Goodwin and K. S. Sin, *Adaptive Filtering Prediction and Control*, 1st ed. New York: Dover, 2009.

[14] M. Abayazid, R. J. Roesthuis, R. Reilink, and S. Misra, "Integrating deflection models and image feedback for real-time flexible needle steering," *IEEE Transactions on Robotics*, vol. 29, no. 2, pp. 542 – 553, 2013.

[15] R. J. Roesthuis, Y. R. J. van Veen, A. Jahya, and S. Misra, "Mechanics of needle-tissue interaction," in *Proceedings of the IEEE Intelligent Robots and Systems (IROS)*, San Francisco, USA, September 2011, pp. 2557 – 2563.

[16] W. Assaad and S. Misra, "Combining ultrasound-based elasticity estimation and FE models to predict 3D target displacement," *Medical Engineering & Physics*, vol. 35, no. 4, pp. 549 – 554, 2013.

[17] A. Gefen and B. Dilmoney, "Mechanics of the normal woman's breast," *Technology and Health Care*, vol. 15, no. 4, pp. 259 – 271, 2007.

[18] T. A. Krouskop, T. M. Wheeler, F. K. B. S. Garra, and T. Hall, "Elastic moduli of breast and prostate tissues under compression," *Ultrasonic Imaging*, vol. 20, no. 4, pp. 260 – 274, 1998.

[19] D. Stoianovici, D. Song, D. Petrisor, D. Ursu, D. Mazilu, M. Mutener, M. Schar, and A. Patriciu, "MRI stealth robot for prostate interventions," *Minimally Invasive Therapy & Allied Technologies*, vol. 16, no. 4, pp. 241 – 248, 2007.